PREDICTION OF INCOMPRESSIBLE FLOW SEPARATION WITH THE APPROXIMATE FACTORIZATION TECHNIQUE

V. MICHELASSI AND C. BENOCCI

von Karman Institute for Fluid Dynamics, Chaussée de Waterloo, 72, B-1640 Rhode Saint Genèse, Belgium

SUMMARY

This paper describes one application of the approximate factorization technique to the solution of incompressible steady viscous flow problems in two dimensions.

The velocity–pressure formulation of the Navier–Stokes equations written in curvilinear non-orthogonal co-ordinates is adopted. The continuity equation is replaced with one equation for the pressure by means of the artificial compressibility concept to obtain a system parabolic in time. The resulting equations are discretized in space with centred finite differences, and the steady state solution obtained by a time-marching ADI method requiring to solve 3×3 block tridiagonal linear systems.

An optimized fourth-order artificial dissipation is introduced to damp the numerical instabilities of the artificial compressibility equation and ensure convergence.

The resulting solver is applied to the prediction of a wide variety of internal flows, including both streamlined boundaries and sharp corners, and fast convergence and good results obtained for all the configurations investigated.

KEY WORDS   Incompressible Flow   Artificial Compressibility   Curvilinear Co-ordinates   Approximate Factorization   Finite Differences   Recirculation

INTRODUCTION

In recent years, the approximate factorization, alternate direction implicit (ADI) technique developed by Beam and Warming[1,2] has been extensively applied to the solution of the compressible Navier–Stokes equations.[3]

The approximate factorization technique presents important advantages with respect to the classical ADI, namely: the flexibility and reduced computational effort[4] following from the choice of the 'delta' formulation; the closer coupling between the different equations of the system, with consequent improvement of the convergence rate, and the easier implementation of boundary conditions. These features make it very attractive also for the solution of the incompressible Navier–Stokes equations, and, indeed, one successful application, using the stream function–vorticity formulation, is reported by Napolitano.[4]

The present authors chose, instead, to investigate the use of this technique for the solution of the primitive variables formulation of the same equations, which is more suitable for eventual extensions to three-dimensional problems.

The use of the artificial compressibility concept[5] made it possible, for steady problems, to write the incompressible, laminar Navier–Stokes equations in a vector form suitable for solution with

the scheme under discussion. Centred finite difference approximations were adopted for all the spatial discretizations.

Preliminary results were obtained on a rectangular mesh,[6] but the final solver was developed in curvilinear non-orthogonal co-ordinates in order to achieve the maximum flexibility in dealing with irregular boundaries.[7]

The resulting code was applied to a variety of flow problems,[8] including both streamlined and bluff obstructions. Satisfactory results were obtained for all the configurations investigated, indicating that a high degree of generality could indeed be achieved. High priority was given to computational efficiency and different options investigated in order to minimize the CPU requirements.

GENERATION OF CO-ORDINATE SYSTEM

An excellent review of the different methods of generating curvilinear meshes was given by Thompson et al.[9] and the relative discussion will not be repeated here. The authors found that the procedure proposed by Thompson et al.[10,11] provided satisfactory grids for all the geometries of interest and used it through all of the present work.

A simply connected flow field in the physical plane x, y is therefore transformed in a rectangle in the mathematical plane ζ, η through the solution of the system of elliptic PDEs[12]

$$\nabla^2 \zeta(x,y) = P(x,y), \quad \nabla^2 \eta(x,y) = Q(x,y), \tag{1}$$

where P and Q are exponential weighting functions which allow one to concentrate mesh points in selected regions of the physical plane.

Different examples of grids generated following the above approach will be shown in the following paragraphs.

Formulation of the equations of motion

The time-dependent, primitive variables (u,v,p) form of the incompressible Navier–Stokes equations is adimensionalized with respect to a velocity scale u_0, length scale l_0 and twice dynamic pressure $\rho_0 u_0^2$, and written in a general system of curvilinear non-orthogonal co-ordinates, maintaining the Cartesian velocity components u and v as dependent variables.

In two dimensions the resulting system is:

Continuity

$$\frac{1}{J}\left(y_\eta \frac{\partial u}{\partial \zeta} - y_\zeta \frac{\partial u}{\partial \eta} + x_\zeta \frac{\partial v}{\partial \eta} - x_\eta \frac{\partial v}{\partial \zeta} \right) = 0; \tag{2}$$

Conservation of momentum in the x direction

$$\frac{\partial u}{\partial t} + \frac{1}{J}\left(y_\eta \frac{\partial u^2}{\partial \zeta} - y_\zeta \frac{\partial u^2}{\partial \eta} \right) + \frac{1}{J}\left(x_\zeta \frac{\partial uv}{\partial \eta} - x_\eta \frac{\partial uv}{\partial \zeta} \right)$$

$$- \frac{1}{ReJ^2}\left(\sigma \frac{\partial u}{\partial \eta} + \tau \frac{\partial u}{\partial \zeta} \right) + \frac{1}{J}\left(y_\eta \frac{\partial p}{\partial \zeta} - y_\zeta \frac{\partial p}{\partial \eta} \right)$$

$$= \frac{1}{ReJ^2}\left(\alpha \frac{\partial^2 u}{\partial \zeta^2} - 2\beta \frac{\partial^2 u}{\partial \zeta \partial \eta} + \gamma \frac{\partial^2 u}{\partial \eta^2} \right); \tag{3}$$

<div align="center">Table I. Metric terms</div>

$J = x_\zeta y_\eta - x_\eta y_\zeta$	$D_x = \alpha x_{\zeta\zeta} - 2\beta x_{\zeta\eta} + \gamma x_{\eta\eta}$
$\alpha = x_\eta^2 + y_\eta^2$	$D_y = \alpha y_{\zeta\zeta} - 2\beta y_{\zeta\eta} + \gamma y_{\eta\eta}$
$\beta = x_\zeta x_\eta + y_\zeta y_\eta$	$\sigma = (y_\zeta D_x - x_\zeta D_y)/J$
$\gamma = x_\zeta^2 + y_\zeta^2$	$\tau = (x_\eta D_y - y_\eta D_x)/J$

Conservation of momentum in the y direction

$$\frac{\partial v}{\partial t} + \frac{1}{J}\left(x_\zeta \frac{\partial v^2}{\partial \eta} - x_\eta \frac{\partial v^2}{\partial \zeta}\right) + \frac{1}{J}\left(y_\eta \frac{\partial uv}{\partial \zeta} - y_\zeta \frac{\partial uv}{\partial \eta}\right)$$

$$- \frac{1}{ReJ^2}\left(\sigma \frac{\partial v}{\partial \eta} + \tau \frac{\partial v}{\partial \zeta}\right) + \frac{1}{J}\left(x_\zeta \frac{\partial p}{\partial \eta} - x_\eta \frac{\partial p}{\partial \zeta}\right)$$

$$= \frac{1}{ReJ^2}\left(\alpha \frac{\partial^2 v}{\partial \zeta^2} - 2\beta \frac{\partial^2 v}{\partial \zeta \partial \eta} + \gamma \frac{\partial^2 v}{\partial \eta^2}\right); \tag{4}$$

where Re is the Reynolds number of the flow. The detailed forms of the different coefficients are given in Table I.

One equation for the pressure is obtained from the time-dependent form of the continuity equation, through the already mentioned artificial compressibility concept:[5] a fictitious state equation, relating pressure to density, is defined as $p = \rho\varepsilon$ (where $\varepsilon > 0$ is the artificial compressibility parameter) and used to replace the density with the pressure, to give

$$\frac{\partial p}{\partial t} + \varepsilon \frac{1}{J}\left(y_\eta \frac{\partial u}{\partial \zeta} - y_\zeta \frac{\partial u}{\partial \eta} + x_\zeta \frac{\partial v}{\partial \eta} - x_\eta \frac{\partial v}{\partial \zeta}\right) = 0, \tag{5}$$

where ε is to be chosen to ensure the fastest convergence to steady state. $\varepsilon \simeq 1$ was found to be the optimal value for the present application.

Replacing equation (2) with (5), the entire system can be cast in a time-dependent form, but obviously, will be valid only at steady state, where $\partial p/\partial t = 0$. The steady state will be attained as the limit of a time-marching process.

For steady flow problems, the use of the artificial compressibility formulation, besides providing a form suitable for the application of the approximate factorization scheme, is, in the experience of the present authors, preferable to the solution of the Poisson equation for the pressure, because it explicitly enforces mass conservation and does not require internal iterations for each step in the fictitious time.

The system including equations (3)–(5) can now be written in compact form:

$$\frac{\partial \mathbf{U}}{\partial t} + \frac{\partial \mathbf{F}}{\partial \zeta} + \frac{\partial \mathbf{G}}{\partial \eta} = \frac{\partial \mathbf{V}_1(\mathbf{U},\mathbf{U}_\zeta)}{\partial \zeta} + \frac{\partial \mathbf{V}_2(\mathbf{U},\mathbf{U}_\eta)}{\partial \zeta} + \frac{\partial \mathbf{W}_1(\mathbf{U},\mathbf{U}_\zeta)}{\partial \eta} + \frac{\partial \mathbf{W}_2(\mathbf{U},\mathbf{U}_\eta)}{\partial \eta}, \tag{6}$$

where $\mathbf{U}$ is the unknown vector, $\mathbf{U}_\zeta$ and $\mathbf{U}_\eta$ are its derivatives along the respective co-ordinate axes, $\mathbf{F}$ and $\mathbf{G}$ are the vectors containing the convective terms and $\mathbf{V}_1$, $\mathbf{V}_2$, $\mathbf{W}_1$ and $\mathbf{W}_2$ are the vectors containing the diffusive terms.

The system is closed with a set of boundary conditions. For the internal flows treated here, these are (Figure 1):
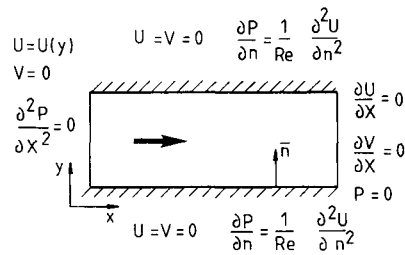
Figure 1. Standard boundary conditions for the internal flow problems

Non-slip on solid walls

$$\frac{\partial p}{\partial n} = \frac{1}{Re}\frac{\partial^2 u_n}{\partial n^2}, \quad u = 0, \quad v = 0, \tag{7}$$

where n is the direction normal to the boundary;

Equilibrium flow at the inlet

$$\partial^2 p/\partial x^2 = 0, \quad u = u(y), \quad v = 0, \tag{8}$$

with an imposed velocity distribution;

Parallel flow at the outlet

$$p = 0, \quad \partial u/\partial x = 0, \quad \partial v/\partial x = 0. \tag{9}$$

SOLUTION SCHEME

The system (6) is solved with a time-marching procedure, where the solutions at two consecutive time steps, n and $n + 1$, are related as

$$\mathbf{U}^{n+1} + \theta\Delta t\left(\frac{\partial \mathbf{F}}{\partial \zeta} + \frac{\partial \mathbf{G}}{\partial \eta} - \frac{\partial \mathbf{V}_1}{\partial \zeta} - \frac{\partial \mathbf{W}_2}{\partial \eta}\right)^{n+1} = \mathbf{U}^n - (1 - \theta)\Delta t$$

$$\times\left(\frac{\partial \mathbf{F}}{\partial \zeta} + \frac{\partial \mathbf{G}}{\partial \eta} - \frac{\partial \mathbf{V}_1}{\partial \zeta} - \frac{\partial \mathbf{W}_2}{\partial \eta}\right)^n + \mathbf{E}^n, \tag{10}$$

where $\frac{1}{2} \leqslant \theta \leqslant 1$ weights the explicit and implicit contribution to the space operator. In the present work θ was kept equal to 1 in order to achieve faster convergence to steady state.

Vectors $\mathbf{F}$, $\mathbf{G}$, $\mathbf{V}_1$ and $\mathbf{W}_2$ must be conveniently linearized in order to be able to solve (10). $\mathbf{E}$ represents a fully explicit term including the vectors $\mathbf{V}_2$ and $\mathbf{W}_1$, which cannot be fitted in a tridiagonal scheme because they contain cross-derivatives. The linearization can be performed without loss of temporal accuracy in the form

$$\bar{\mathbf{F}}^{n+1} = \mathbf{F}^n + A^n(\mathbf{U}^{n+1} - \mathbf{U}^n), \tag{11}$$

$$\mathbf{G}^{n+1} = \mathbf{G}^n + B^n(\mathbf{U}^{n+1} - \mathbf{U}^n), \tag{12}$$

$$\mathbf{V}_1^{n+1} = \mathbf{V}_1^n + (P - R_\zeta)^n(\mathbf{U}^{n+1} - \mathbf{U}^n) + (\partial R^n/\partial \zeta)(\mathbf{U}^{n+1} - \mathbf{U}^n), \tag{13}$$

$$\mathbf{W}_2^{n+1} = \mathbf{W}_2^n + (Q - S_\eta)^n(\mathbf{U}^{n+1} - \mathbf{U}^n) + (\partial S^n/\partial \eta)(\mathbf{U}^{n+1} - \mathbf{U}^n), \tag{14}$$

where

$$A = (\partial \mathbf{F}/\partial \mathbf{U}), \quad B = (\partial \mathbf{G}/\partial \mathbf{U}), \quad P = (\partial \mathbf{V}_1/\partial \mathbf{U}), \quad R = (\partial \mathbf{V}_1/\partial \mathbf{U}_\zeta),$$

$$R_\zeta = (\partial R/\partial \zeta), \quad Q = (\partial \mathbf{W}_2/\partial \mathbf{U}), \quad S = (\partial \mathbf{W}_2/\partial \mathbf{U}_\eta); \quad S_\eta = (\partial S/\partial \eta).$$

Putting (11)–(14) into (10) and adopting the operator of forward differencing in time $\Delta \mathbf{U}$ ('delta' form),

$$\Delta \mathbf{U}^{n+1} = \mathbf{U}^{n+1} - \mathbf{U}^n, \tag{15}$$

the following system in the unknown $\Delta \mathbf{U}$ is obtained:

$$\left[\mathbf{I} + \theta \Delta t \left(\frac{\partial A^n}{\partial \zeta} - \frac{\partial^2 R^n}{\partial \zeta^2} + \frac{\partial B^n}{\partial \eta} - \frac{\partial^2 S^n}{\partial \eta^2} \right) \right] \Delta \mathbf{U}^n$$

$$= -\Delta t \left(\frac{\partial \mathbf{F}}{\partial \zeta} + \frac{\partial \mathbf{G}}{\partial \eta} - \frac{\partial \mathbf{V}_1}{\partial \zeta} - \frac{\partial \mathbf{W}_2}{\partial \eta} \right) + \mathbf{E}^n = \text{RHS} \tag{16}$$

where $\mathbf{I}$ is the identity matrix and RHS stands for right-hand side.

The original two-dimensional problem is split into two one-dimensional problems, without any loss of accuracy in time, through the approximate factorization

$$\left[\mathbf{I} + \theta \Delta t \left(\frac{\partial A^n}{\partial \zeta} - \frac{\partial^2 R^n}{\partial \zeta^2} \right) \right] \left[\mathbf{I} + \theta \Delta t \left(\frac{\partial B^n}{\partial \eta} - \frac{\partial^2 S^n}{\partial \eta^2} \right) \right] \Delta \mathbf{U}^n = \text{RHS}. \tag{17}$$

The introduction of an intermediate unknown $\Delta \mathbf{U}^*$, defined as

$$\Delta \mathbf{U}^* = \left[\mathbf{I} + \theta \Delta t \left(\frac{\partial B^n}{\partial \eta} - \frac{\partial^2 S^n}{\partial \eta^2} \right) \right] \Delta \mathbf{U}, \tag{18}$$

makes it possible to implement an alternating direction sequence, solving first (17) in the unknown $\Delta \mathbf{U}^*$ and then (18) in the unknown $\Delta \mathbf{U}$; each of the two steps requires only the solution of a block-tridiagonal system. The steady state is reached as the limit of the time-marching procedure.

Among the advantages offered by the approximate factorization with respect to the classical ADI methods, first proposed by Peaceman and Rachford,[13] is the fact all the intermediate steps are consistent with the original PDEs (3)–(5), so that the boundary conditions for $\Delta \mathbf{U}^*$ and $\Delta \mathbf{U}$ are exactly the same as for $\mathbf{U}$ and their implementation is immediate.

In order to simplify the numerical treatment, the boundary conditions are imposed explicitly. System (17) is solved for time step $n + 1$ with $\Delta \mathbf{U}^* = \Delta \mathbf{U} = 0$ at the boundaries and the boundary values updated afterwards using the new values for the inner field. Such a choice was found to have no adverse effect on the stability of the solution.

DISCRETIZATION

Grid layout for the dependent variables

System (18) is discretized over a non-staggered mesh. Such a choice is motivated by the difficulty of generating properly a staggered mesh in curvilinear co-ordinates and, above all, by the need to obtain a system of discrete equations easy to fit in a tridiagonal scheme.

It is well known (and a very clear presentation of the whole problem can be found in Reference 7), that numerical problems can be expected when a non-staggered mesh is used for the discretization of the Navier–Stokes equations in the primitive variables formulation. This follows from the fact that the pressure at point i, j does not explicitly appear in the calculation of the velocity

components at i, j and there is therefore no direct coupling between the computed pressures at adjacent nodes (only a weak coupling is provided by the boundary conditions). Consequently, pressures at odd and even points can converge to two different solutions, resulting in the typical 'chessboard' pattern. Such behaviour does not necessarily prevent the attainment of a fully converged solution for the velocity, but results in wiggles on the pressure. The present authors performed a careful numerical study of the extent of such a problem and, above all, of the role of the boundary conditions. It was found[14] that solutions practically free of wiggles could be found, for all the problems investigated, by discretizing equations (7)–(9) with second-order, one-sided finite differences.

Discrete equations

All the space derivatives that appear in equations (3)–(5) are discretized with centred, second-order-accurate finite differences.

In order to prevent the well-known problems related to the centred discretization of the advection terms, the guidelines suggested by Gresho and Lee[15] were followed, and the grid spacings controlled to achieve mesh Reynolds number smaller than 2 in all the regions where strong gradients are expected. Stable and wiggle-free solutions were obtained without the need to introduce damping terms in the momentum equations.

On the contrary, the introduction of artificial damping was found necessary to ensure convergence of the artificial compressibility equation. Equation (5) is fundamentally an explicit relationship for the pressure which does not include any physical diffusive or dissipative term and is, therefore, sensitive to numerical perturbations. This problem does not appear when the artificial compressibility is coupled to an explicit solver (as in the original work by Chorin[5]) or when it is used as a 'corrector' step after the solution of the momentum equations, but it is fundamental for the present approach, where an implicit coupled solver is to be used.

In fact, with the present discretization,[1,2] the numerical modes with the highest wave numbers are entirely undamped and may easily lead to instabilities. Such a behaviour was observed for any flow geometry more complex than a straight channel and led to the decision to add an artificial dissipation term to equation (5).

Beam and Warming [1,2] propose to increase the stability of the approximate factorization technique by adding to the basic equations fourth-order artificial dissipation terms in the form of fourth-order derivatives of the basic unknowns. In vectorial form the final system becomes:

$$\frac{\partial \mathbf{U}}{\partial t} + \frac{\partial \mathbf{F}}{\partial \zeta} + \frac{\partial \mathbf{G}}{\partial \eta} = \frac{\partial \mathbf{V}_1}{v\zeta} + \frac{\partial \mathbf{V}_2}{\partial \zeta} + \frac{\partial \mathbf{W}_1}{\partial \eta} + \frac{\partial \mathbf{W}_2}{\partial \eta} - \frac{\Delta\zeta^4}{8}\frac{\partial^4 \mathbf{U}}{\partial \zeta^4}\Omega_\zeta - \frac{\Delta\eta^4}{8}\frac{\partial^4 \mathbf{U}}{\partial \eta^4}\Omega_\eta, \qquad (19)$$

where the additional terms can be weighted according to the constants Ω_ζ and Ω_η.

The terms so introduced will be $O(\Delta\zeta^4)$ or $O(\Delta\eta^4)$, while the physical terms are discretized to $O(\Delta\zeta^2)$ or $O(\Delta\eta^2)$: in this way the formal accuracy of the method is not disrupted. These terms are treated in a fully explicit way in order to maintain the tridiagonality of the block matrix to be inverted. Therefore, there will be an explicit limit for the maximum allowed values of Ω_ζ and Ω_η.

On the basis of a linear stability analysis of model equations[3] for an unbounded domain, the limit $\Omega_\zeta < 1, \Omega_\eta < 1$ is proposed.[1]

However, the present authors found that better results in terms of mass conservation and convergence speed could be obtained, especially for geometries including sharp corners, by introducing non-uniform weights and so confining the influence of the dissipative terms to the high-gradient regions where the strongest instabilities are likely to occur. Two new weighting functions $\Omega_\zeta(i, j)$ and $\Omega_\eta(i, j)$ are introduced to weight individually the artificial dissipation terms at

each mesh point i, j,

$$\Omega_\zeta(i,j) = \Omega_\zeta' \frac{|\mathbf{U}(i+1,j) - \mathbf{U}(i-1,j)|}{|\zeta(i+1,j) - \zeta(i-1,j)|}, \quad \Omega_\eta(i,j) = \Omega_\eta' \frac{|\mathbf{U}(i,j+1) - \mathbf{U}(i,j-1)|}{|\eta(i,j+1) - \eta(i,j-1)|}, \tag{20}$$

while the above-mentioned stability criterion becomes $\Omega_\zeta(i,j) < 1, \Omega_\eta(i,j) < 1$.

The weights introduced by (20) are directly proportional to the change of the physical quantity and inversely proportional to the grid spacing, so that artificial dissipation is introduced only in high-gradient regions. In Figure 2 a comparison between the normal 'constant weight mode' and

(a)

(b)
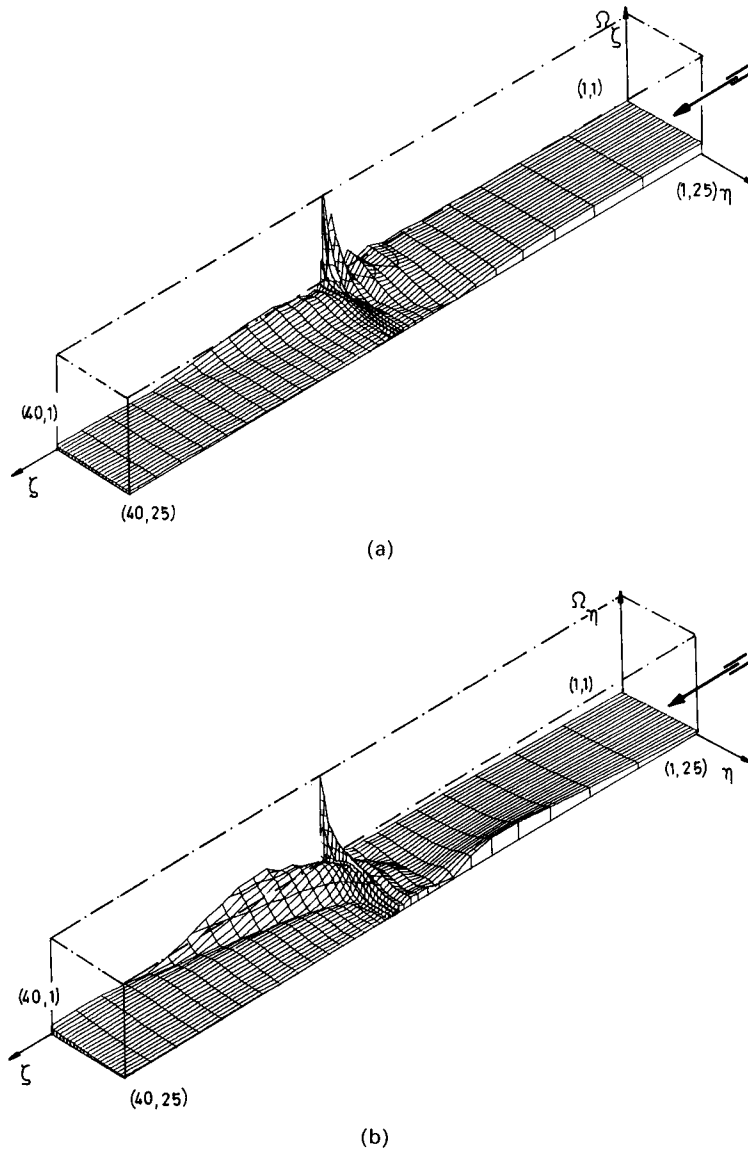
Figure 2. Weights distribution for the artificial dissipation term: backward facing step—case 2 computational domain; —·—·— constant weight; ——— variable weight. (a) ζ-direction weight for pressure; (b) η-direction weight for pressure

the new proposed 'variable weight mode' is shown for the backward-facing step problem of Reference 16, case 2.

In the figure the computational domain in the ζ and η axes is plotted on the horizontal plane and the vertical axis represents the applied weight for the fourth-order terms. For the case considered, the weight ranges from 0·01 in smooth flow regions to 0·8 close to the separation point; in the constant weight mode the weight factor would remain equal to 0·8 everywhere in the domain. It is therefore possible to introduce locally a strong damping, while maintaining a weak one in smooth flow regions.

This formulation was applied to obtain the results to be discussed in the next section.

Time step choice

The formulation adopted for the present work is fully implicit and, therefore, unconditionally stable at least for linear problems with periodic boundary conditions.[1] As the steady state is the only result sought, accuracy in time is not a problem and it is possible to work with the time step or, to be more precise, with the CFL (Courant–Friedrich–Levy) number yielding fastest convergence. It has to be remarked that the largest CFL compatible with the practical problems of non-linear instability of the Navier–Stokes equations is not necessarily the optimal one for convergence to the steady state solution,[17] so that a careful optimization is required.

For the present work, the following definition is taken for the CFL[18] (in terms of the adimensional variables):

$$CFL = \frac{\Delta t}{\dfrac{\Delta\zeta/2}{|\mathbf{u}| + \sqrt{\varepsilon + 2/Re_\zeta}} + \dfrac{\Delta\eta/2}{|\mathbf{v}| + \sqrt{\varepsilon + 2/Re_\eta}}}, \tag{21}$$

where Δt is the time step and Re_ζ and Re_η are the Reynolds numbers based upon the local mesh spacing.

For a non-uniform flow and even more for a non-uniform and highly distorted mesh, the local CFLs for a fixed Δt change considerably; therefore, if a reasonable upper limit on the CFL is to be respected in the high-gradient regions, the CFLs in smooth flow regions are likely to be very small and, in fact, full advantage of the implicit formulation is not taken.

Therefore, for steady state problems, it is more attractive to vary the time step from mesh point to mesh point [3–18] to keep the CFL approximately constant all over the mesh and to ensure a more uniform convergence rate.

A variable-time-step/constant-CFL formulation could be obtained by solving equation (21) for the unknown Δt; alternatively, a simpler and computationally less expensive formulation, leading to an approximately constant CFL, is proposed in Reference 3:

$$\Delta t = \frac{\Delta t_{\text{ref}}}{|\mathbf{u}| + |\mathbf{v}| + [\varepsilon(\zeta_x^2 + \zeta_y^2 + \eta_x^2 + \eta_y^2)]^{1/2}}, \tag{22}$$

where Δt_{ref} is a reference time step.

Both formulations were tested, and the best overall results obtained with (22). Comparison of convergence histories for 'standard' approximate factorization solutions, with both artificial dissipation coefficients and time step constant in space, and the present one, including equations (20) and (22), did show, typically, a decrease in size of the residual by about two orders of magnitude for a fixed number of iterations.[8] Moreover, with the optimized formulation, the residual could easily be brought down to machine accuracy.

APPLICATIONS

As already anticipated, the goal of the present work is to develop a solver able to deal with a wide variety of flow problems. Therefore, a large number of tests were performed for geometries including both streamlined boundaries and sharp corners,[8] and the most representative results will now be discussed. All the calculations were performed on a VAX 780-11 computer.

Diverging channels

The first case investigated was the diverging channel shown in Figure 3, whose wall geometry is defined by the law

$$y_{\text{wall}} = [\tanh(2 - 30x/Re) - \tanh(2)]/2,$$

which has been proposed as a benchmark case by Napolitano and Orlandi.[19]

As required by the benchmark, the problem was studied for Reynolds numbers (based on the maximum inlet velocity and on the inlet width) of 10 and 100, for the boundary conditions shown in Figure 3, and a mesh of 21×21 points.

For both configurations, convergence to a maximum local residual of 10^{-4} for the pressure was obtained in about 300 iterations for a CPU time of 13 min; mass flow rate along the channel was conserved with an error of about 1%, which is mostly due to the fact that mass conservation is not explicitly imposed on the solid boundaries.[14]

In both cases, the existence of a small separated region is predicted by the present solver. The inlet velocity profile is shown in Figure 4, together with calculated velocity profiles for the separated region and the following reattachment.

One of the quantities proposed for the benchmark, namely the pressure on the lower wall, is presented in Figure 5 for the case $Re = 10$ and in Figure 6 for the case $Re = 100$, together with numerical results from Reference 19. The present results fall well within the spread of the other ones available and satisfactorily close to the ones obtained by Cliffe et al., which are considered to be the best ones available by the authors of the benchmark.[19] The discrepancy in the pressure values near the outlet section, which can be observed in Figure 6, is due to the adoption of the boundary condition $\partial p/\partial y = 0$ instead of the fixed pressure demanded by the benchmark; the change did result in a smoother solution in the outlet region.

Channels with curved walls

A second test for internal flows with streamlined boundaries was performed by investigating the family of curved channels proposed by Ghia et al.[20] as a test of the ability of incompressible Navier–Stokes solvers to detect recirculation in complex geometries.
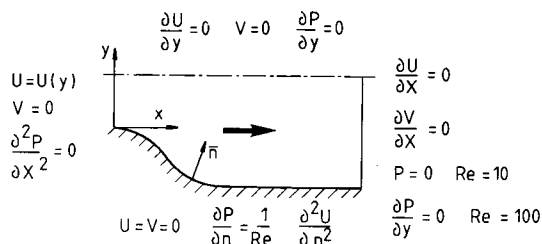
Figure 3. Geometry and boundary conditions for the diverging channel problem
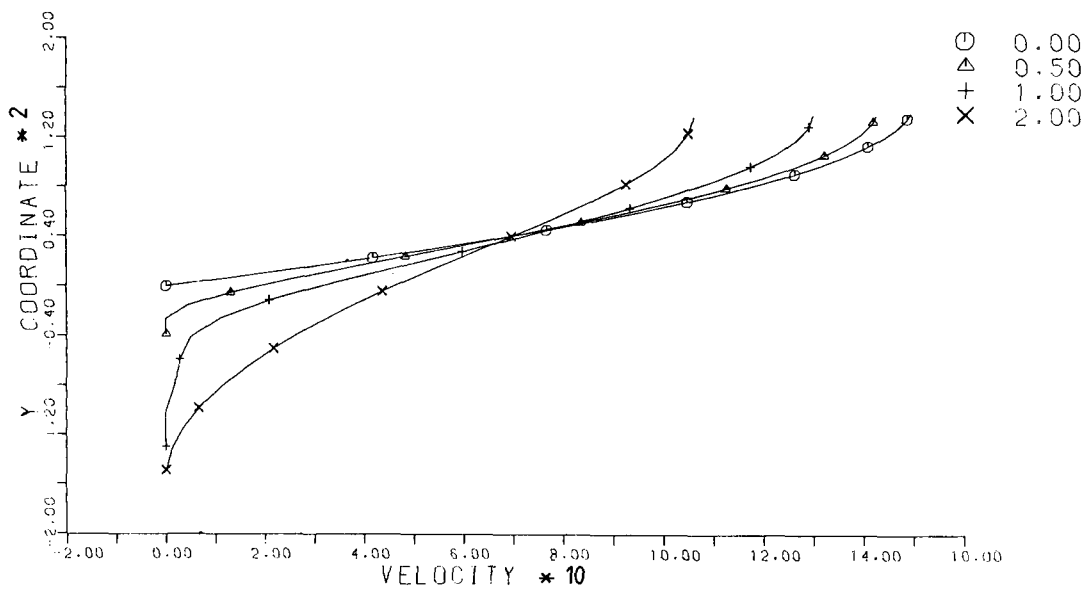
Figure 4. Velocity profiles in the separation region for the case $Re = 10$
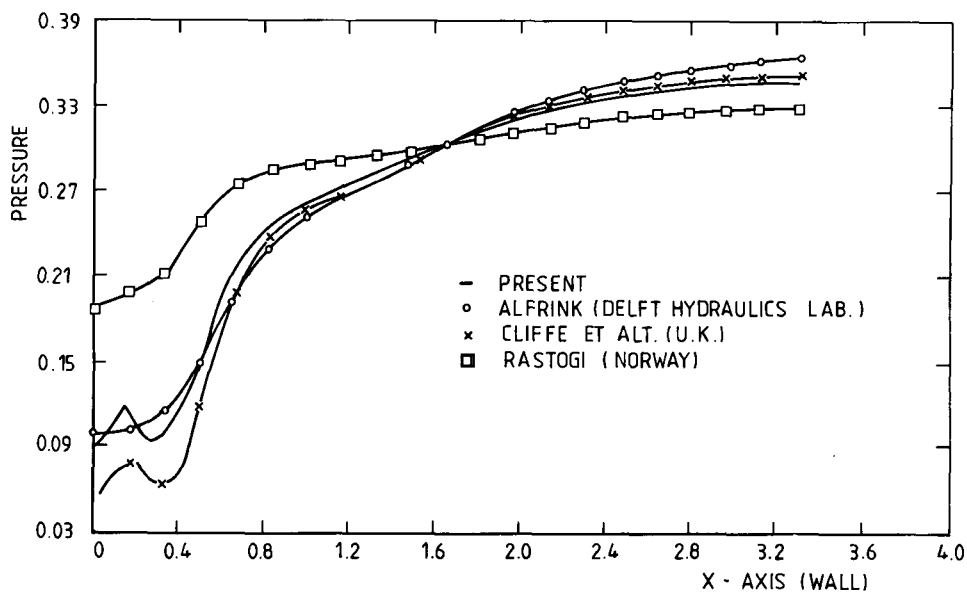
Figure 5. Comparison of predicted [19] pressure distributions on the wall for the case $Re = 10$

The wall shapes are defined by the equations

$$y_0 = (a^2 - \Delta^2)/\Delta,$$

$$y\frac{x^2 + y^2 - a^2}{x^2 + y^2} - y_0 = 0 \text{ for the lower wall, 1 for the upper wall.}$$

The curvatures are defined by the set of parameters a^2 and Δ; the values corresponding to the
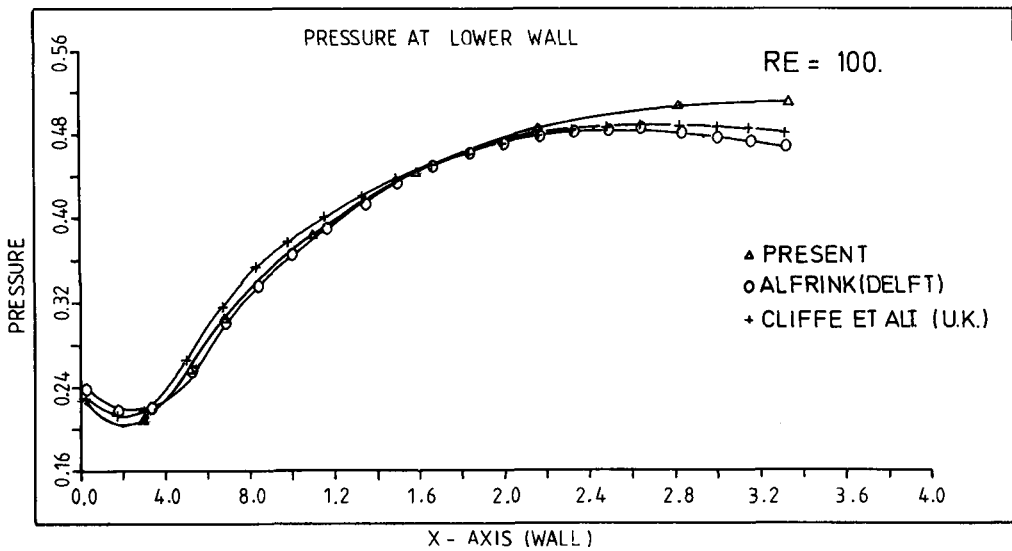
Figure 6. Comparison of predicted[19] pressure distributions on the wall for the case $Re = 100$

Table II. Curved channel—parameters set

Case	1	2	3	4
a^2	0·210	0·585	0·644	0·725
Δ	0·782	0·678	0·643	0·606

cases investigated are reported in Table II. The shape of the resulting channel, together with a typical mesh, can be seen in Figure 7.

All the calculations were performed for a Reynolds number (based on the inlet width and the maximum inlet velocity) equal to 100 and the boundary conditions defined in the previous section. Two meshes were tested: a coarse one made by 40 × 20 points and a refined one of 61 × 21 points.

For the refined mesh, convergence down to 10^{-5} residual error was obtained in less than 600 iterations for all four cases, corresponding to a CPU time of about 60 min, while the mass error remained around 1%.

Predicted velocity profiles for case 4 are shown in Figure 8, starting from the symmetry axis: the separated region and following reattachment are well in evidence.

The overall results are quite close to the one presented in Reference 20 for the same number of mesh points, as can be seen from the comparison between predicted recirculation lengths in Table III.

The only significant discrepancy is that the present solver does not predict separation for case 1; the flow is, however, very close to separation, as can be seen by comparing the predicted values of the 'pressure parameter' obtained by subtracting from the computed wall pressure the corresponding value for a straight channel. The results for cases 1 and 4 are shown in Figures 9 and 10 and the general agreement appears acceptable.

It can therefore be concluded that the present solver predicts correctly and efficiently most separated flows in channels with streamlined walls, and the scope of the investigation can be extended to the solution of problems including separation on sharp corners.
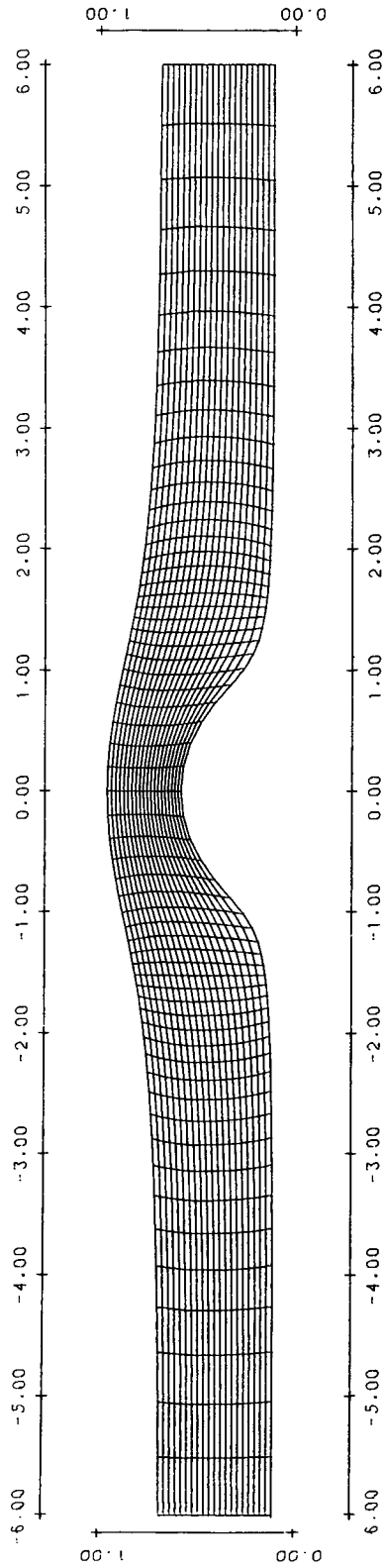
Figure 7. Typical geometry and mesh for the curved channel problem: case 4. Mesh points $= 61 \times 21$; $Re = 100$
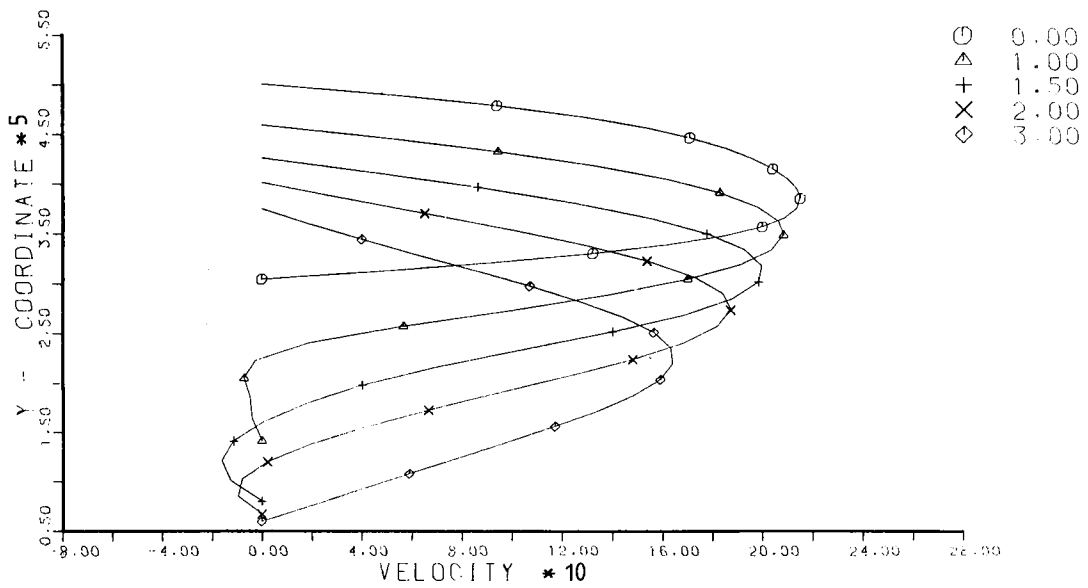
Figure 8. Velocity profiles in the separation and reattachment region: case 4

Table III. Curved channel separation and reattachment points in wall co-ordinates (estimated from plotted streamlines for values from Reference 20)

Case	Separation point		Reattachment point	
	Present	Ref. 20	Present	Ref. 20
1	—	0·7	—	1·32
2	0·95	0·87	1·95	2·0
3	0·55	0·46	2·10	2·16
4	0·46	0·43	2·30	2·42
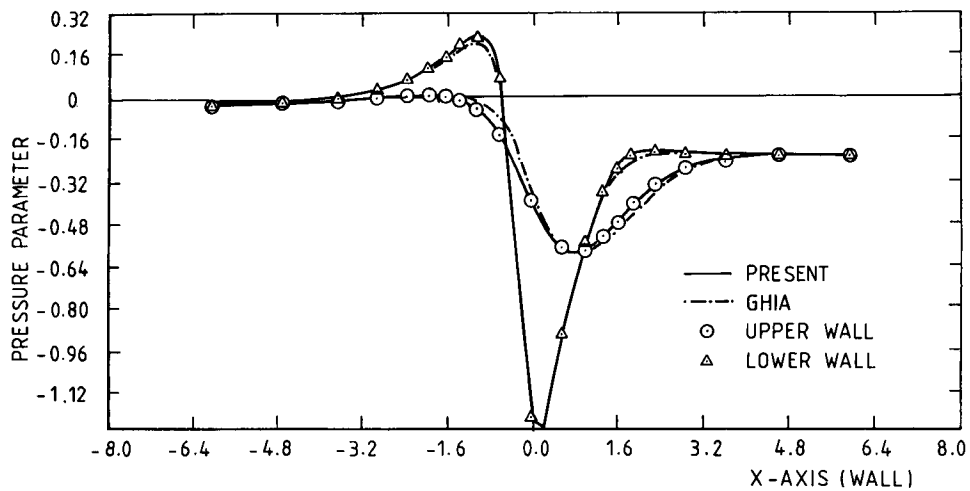
Figure 9. Comparison of predicted[20] pressure parameters: case 1
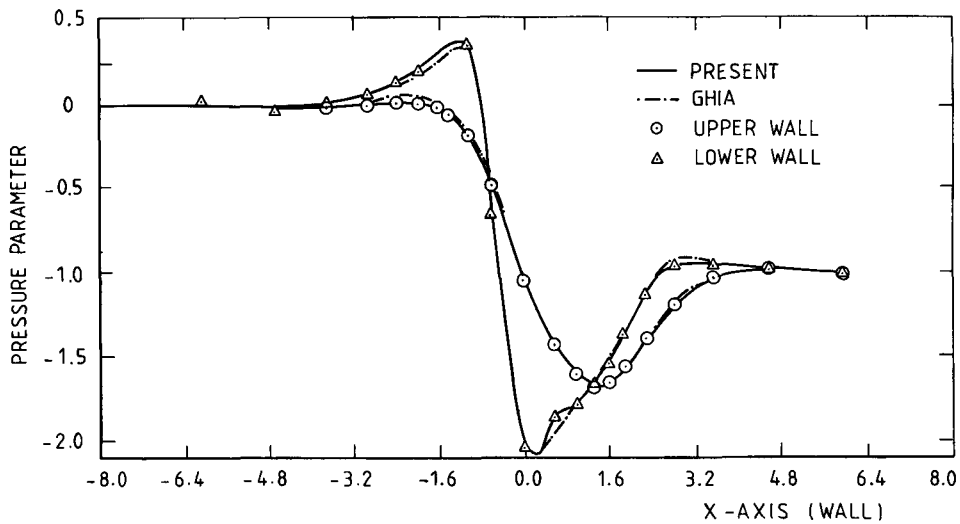
Figure 10. Comparison of predicted[20] pressure parameters: case 4

Backward-facing steps

In view of the large amount of available literature and its interest from the numerical point of view, the problem of flow over a backward-facing step was selected as the fundamental test case to assess the performances of the solver for geometries including sharp corners.

The cases studied are the ones proposed for a GAMM workshop[16] for which both experimental and numerical results are available for comparison.

The four test cases cover two inlet/outlet ratios— namely $h/H = 0.333$ and $h/H = 0.5$, where h is the height of the step and H that of the channel outlet section—and two values of the Reynolds number (based on the maximum inlet velocity and inlet width), $Re = 50$ and $Re = 150$.

The geometry of the problem, together with a typical mesh, is presented in Figure 11. Three different meshes, made respectively of $51 \times 21, 61 \times 25$ and 70×39 points, were tested; while the coarsest mesh already gave results comparable to the ones presented in Reference 16, a significant improvement in the prediction of some critical parameters (see Table IV below), as well an important decrease in mass error, was found with the most refined mesh.

For the coarsest mesh, full convergence down to 10^{-7}–10^{-8} residuals was reached in less than 1000 iterations, with a mass error of the order of 1.3%; for the more refined mesh, between 2400 and 3000 iterations were required to achieve a comparable convergence level and the mass error reduced to around 0.4%. The corresponding CPU time ranged between 100 and 600 min.

The cases treated are summarised in Table IV, together with the predicted values of two benchmark quantities, namely the reattachment length and the minimum value of the stream function in the centre of the recirculation bubble; the experimental values and the spread of the other available numerical results reported in Reference 16 are also given comparison. Good agreement can be observed, with the present values falling well within the spread of the numerical results and satisfactorily close to the experimental ones. Two different values are presented for the 'experimental' stream function, as reported in two different analysis of the experimental results; the present authors consider that this discrepancy can give the reader a fair idea of the uncertainty level attached to the present comparison and its interpretation.

An example of predicted velocity profiles (case 3) is presented in Figure 12, showing results for the separation bubble and the following reattachment region; the agreement with the experimental data appears satisfactory.
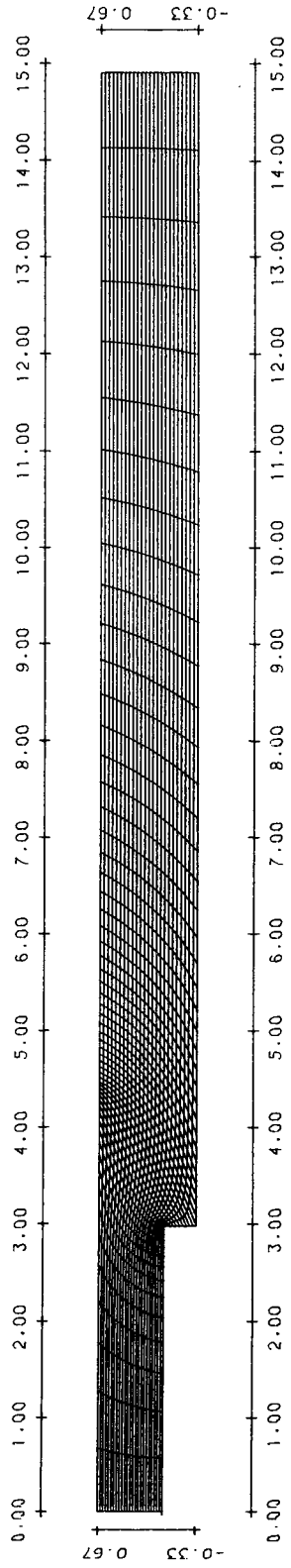
Figure 11. Typical geometry and mesh for the backward-facing step problem. Mesh points = 61 × 25; $Re = 50$

Table IV. Analysis of laminar flow over a backward-facing step: a GAMM workshop

Case	Re	h/H	Reattachment length*			Stream function	
			Present	Num.[16]	Exp.[16]	Present	Exp.[16]
1	50	1/3	2·6 c	1·56–3·1	3	0·018 c	0·012–0·018
			2·8 r			0·017 r	
2	50	1/2	2·0 c	1·56–2·75	—	0·033 c	—
			2·3 r			0·030 r	
3	150	1/3	5·6 c	4·69–7·25	6	0·025 c	0·016–0·024
			6·0 r			0·020 r	
4	150	1/2	4·4 c	3·7–5·8	4·5	0·063 c	0·057–0·086
			4·5 r			0·060 r	

* Adimensionalized by step height. c. coarse mesh. r. refined mesh.
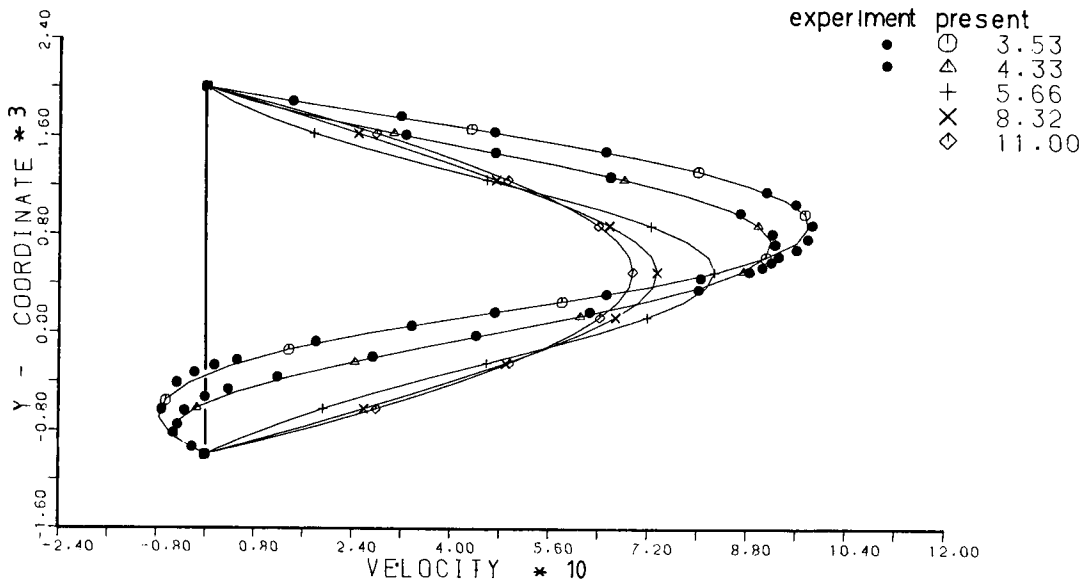
Figure 12. Velocity profiles in the separation and reattachment region: case 3

Figures 13–15 present a comparison between predicted and measured shear stresses on the lower wall for the three cases where experimental data are available. The agreement appears good, with the partial exception of case 4 (Figure 15) where the prediction does not show the wall shear stress overshoot following reattachment; this tendency is shared with most of the other numerical solutions presented in Reference 16. An overshoot in wall shear stress is predicted by the present solver only at higher values of the Reynolds number.[6]

Steps of rectangular cross-section

In order to complete the present analysis, the flow around an obstacle of rectangular cross-section was also considered. Three different geometries, reported in Table V as cases 1, 2 and 3, were studied: they cover a variety of aspect ratios (h/H and h/l, where h is the height of the obstacle, l
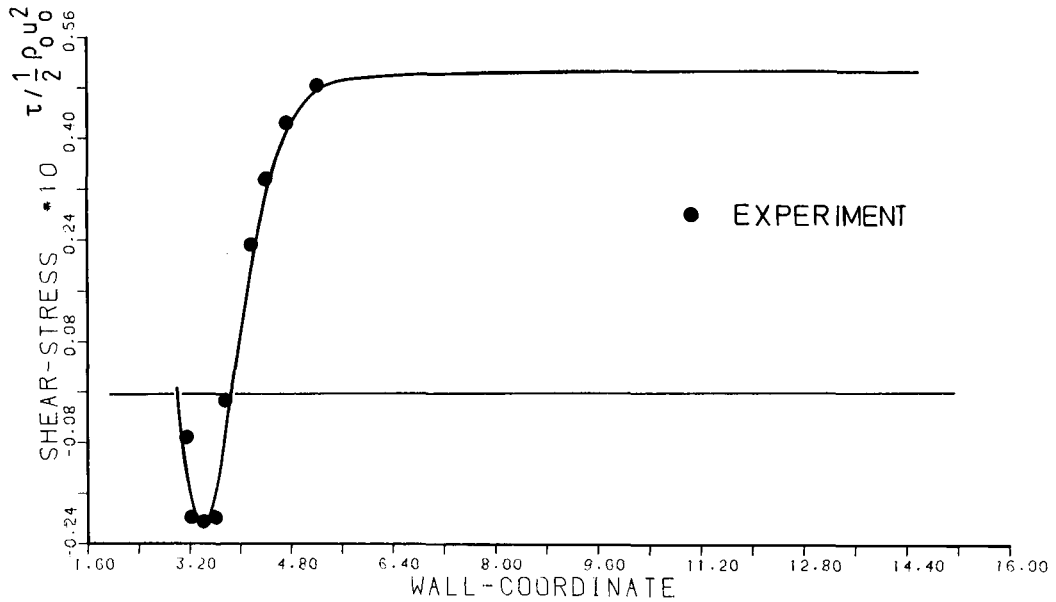
Figure 13. Comparison of predicted and measured[16] wall shear stress on the lower wall: case 1
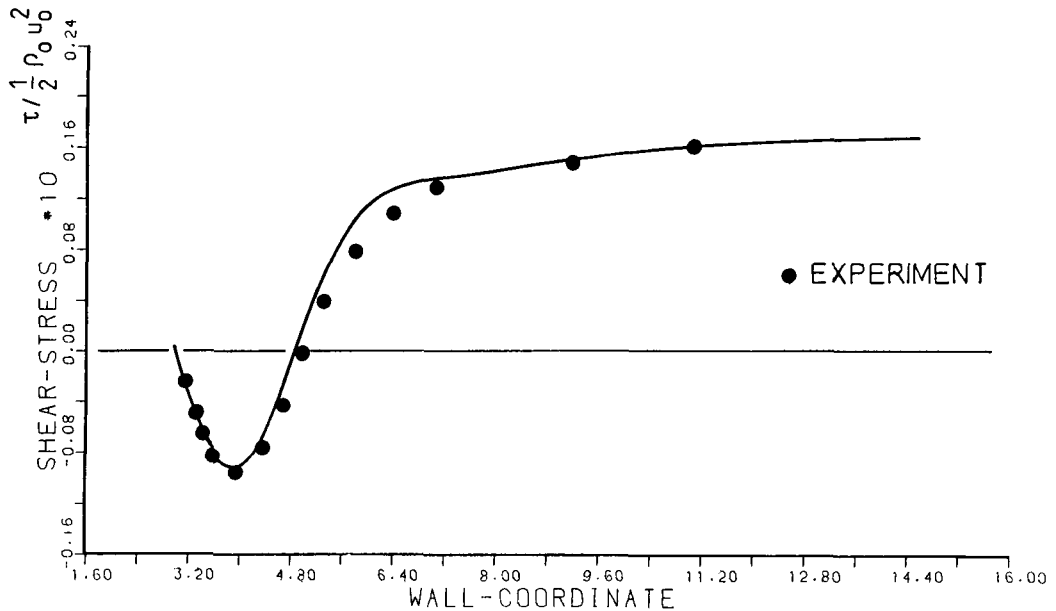
Figure 14. Comparison of predicted and measured[16] wall shear stress on the lower wall: case 3

its length and H the height of the channel) and two different Reynolds numbers (based on the channel inlet section height and the maximum inlet velocity). For case 1 and 2, experimental results are available in the literature[21] and were used for comparison (the uncertainty in test Reynolds number and results is estimated as 6%); for case 3, the present results were compared with another numerical solution.[22]
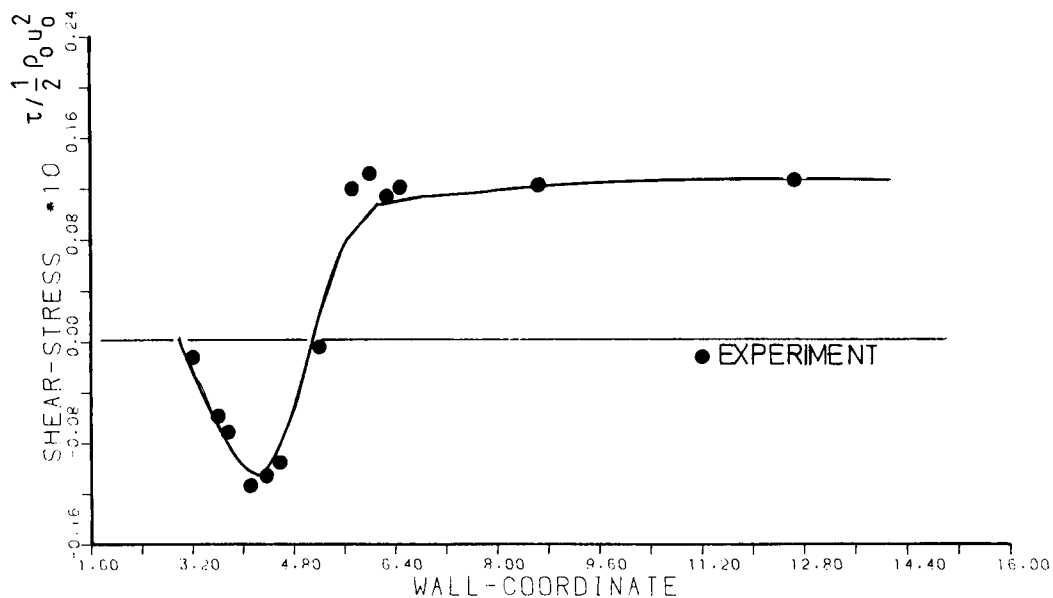
Figure 15. Comparison of predicted and measured[16] wall shear stress on the lower wall: case 4

Table V. Analysis of laminar flow over a step

Case	Re	h/H	h/l	Reattachment length*		Streamfunction	
				Present	Liter.	Present	Liter.
1	144	0·5	2·5	6·2	7·5[21]	0·115	—
2	144	0·5	0·25	6·1	7·0[21]	0·070	—
3	85	0·4	1·0	3·5	3·6[22]	0·035	0·028[22]

* Adimensionalized by step height

For all three cases, a mesh mode of 70×25 points was adopted. The grid for case 2 is shown as an example in Figure 16.

Convergence was found to be very slow, especially because of the very high flow gradients around the upstream concave corner: 2000 iterations, corresponding to 280 min of CPU times were needed to bring case 1 to a 10^{-3} residual and 5% mass error; the same number of iterations did bring to full convergence with a 10^{-6} residual and 3% mass error for case 2 and to a comparable residual and 2% mass error for case 3. These results clearly show that case 1 represents the limit of the geometries which can be treated successfully with the present mesh generator.

It has to be remarked that it was impossible to detect the small recirculation bubble upstream of the obstacle, because its size is of the same order as the mesh resolution which could be achieved. (The bubble was found in calculations employing the same scheme, but for a 75×51 Cartesian mesh, by one of the present authors.[6])

The comparison between the results of the present solver and the aforementioned references for the value of the reattachment length downstream of the obstacle and, where possible, for the stream function at the centre of the recirculation bubble is presented in Table V.

The agreement is markedly worse than the previous cases, but still acceptable in view, above all, of the uncertainty in the experimental results.
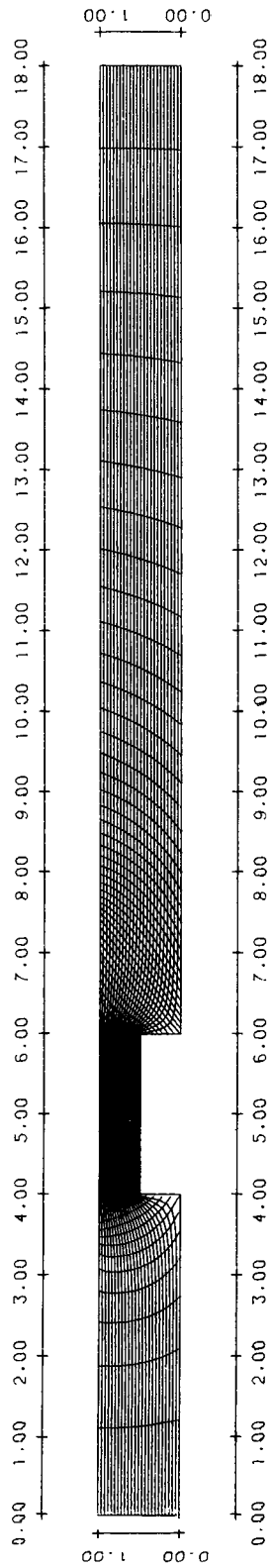
Figure 16. Typical geometry and mesh for obstruction of rectangular cross-section: case 2. Mesh points $= 70 \times 25$; $Re = 144$
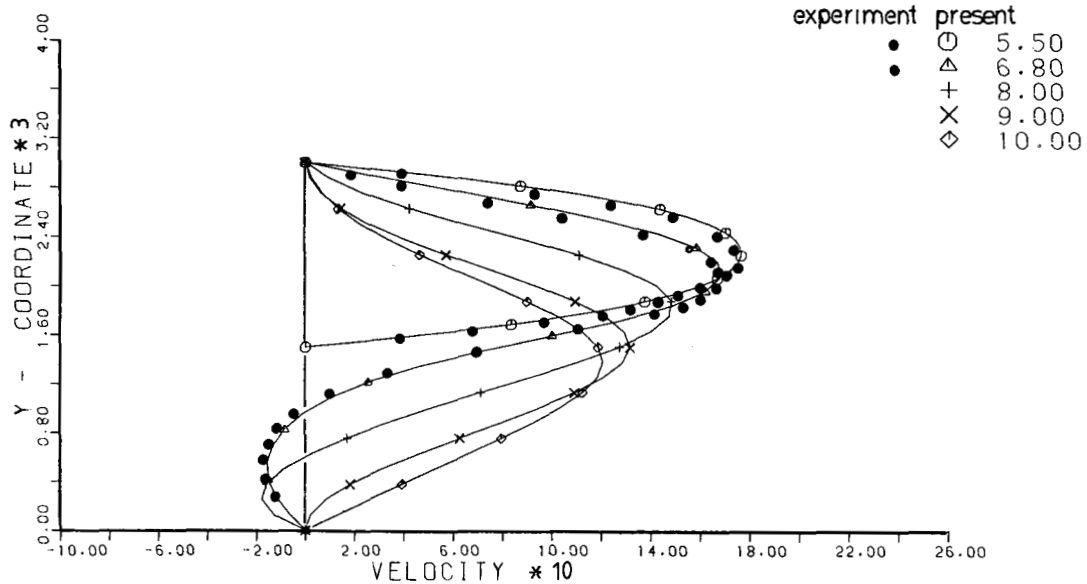
Figure 17. Velocity profiles in the separation and reattachment region

Velocity profiles for case 2 are shown in Figure 17: velocity profiles above the obstacle and in the recirculation region are compared with the experimental ones, and the agreement appears satisfactory.

CONCLUSIONS

A general implicit solver for the laminar, incompressible, steady state Navier–Stokes equations was developed. The approximate factorization method proposed by Beam and Warming, together with the artificial compressibility formulation and the adoption of curvilinear non-orthogonal co-ordinates, proved itself an efficient way of solving a wide range of internal flow problems.

Introduction of an optimized fourth-order numerical dissipation and a variable time step allowed acceptable results to be achieved even for every complex configurations and brought a significant increase in the speed of convergence.

The only significant discrepancy with the results used as a benchmark was found for channel 1 of Reference 20, where no separation is predicted by the present solver. In the opinion of the authors, the disagreement is due to the lower accuracy of the boundary condition adopted in the present work for the pressure and indicates a need for improvement in this area.

The limitations connected to the use of a general co-ordinate generator clearly emerge when geometries including sharp corners are considered: for the flow around a step of rectangular cross-section, the results appear worse than the ones obtained by one of the present authors with a comparable computational effort over a Cartesian mesh. However, it is the opinion of the authors that the decrease in performance remains an acceptable price to pay for the generality of the code.

REFERENCES

1. R. M. Beam and R. F. Warming, 'Implicit numerical methods for the compressible Navier–Stokes and Euler equations', *LS 1982-04, Computational Fluid Dynamics*, von Karman Institute, April 1982.
2. R. M. Beam and R. F. Warming, 'An implicit factored scheme for the compressible Navier–Stokes equations', *AIAA J.*, **16**, 393–402 (1978).

3. T. H. Pulliam, 'Efficient solution methods for the Navier–Stokes equations', *LS1986-02, Numerical Techniques for Viscous Flow Solutions in Turbomachinery Bladings*, von Karman Institute, January 1986.
4. M. Napolitano, 'Efficient ADI and spline ADI methods for the steady state Navier–Stokes equations', *Int. j. numer. methods fluids*, **4**, 1101–1115 (1984).
5. A. J. Chorin, 'A numerical method for solving incompressible viscous flow problems', *J. Comput. Phys.*, **2**, 12–21 (1967).
6. C. Benocci and N. Ceresola, 'Solution of the incompressible Navier–Stokes equations with the approximate factorization technique', *Technical Memorandum 39*, von Karman Institute, December 1985.
7. C. R. Maliska and G. D. Raithby, 'A method for computing three dimensional flows using non-orthogonal boundary fitted coordinates', *Int. j. numer. methods fluids*, **4**, 519–537 (1984).
8. V. Michelassi and C. Benocci, 'Solution of the incompressible Navier–Stokes equations in curvilinear non-orthogonal coordinates', *Technical Note 158*, von Karman Institute, September 1986.
9. J. F. Thompson, Z. U. A. Warsi and C. W. Mastin, 'Boundary fitted coordinate systems for numerical solution of partial differential equations. A review', *J. Comput. Phys.* **47**, 1–108 (1982).
10. J. F. Thompson, F. C. Thames and C. W. Mastin, 'Automatic numerical generation of body fitted curvilinear coordinate system for fields containing any number of arbitrary two dimensional bodies', *J. Comput. Phys.*, **15**, 299–319 (1974).
11. J. F. Thompson, 'Numerical solution of flow problems using body-fitted coordinate systems', in W. Kollman (ed.), *Computational Fluid Dynamics*, Hemisphere, Washington, 1980, pp. 1–98.
12. J. F. Thompson, F. C. Thames and C. W. Mastin, 'Boundary fitted curvilinear coordinate systems for solution of partial differential equations on fields containing any number of arbitrary two dimensional bodies', *NASA CR 2729*, July 1977.
13. D. W. Peaceman and H. H. Rachford, 'The numerical solution of parabolic and elliptic partial differential equations', *J. Soc. Indust. Appl. Math.*, **3**, 28–41 (1955).
14. V. Michelassi and C. Benocci, 'The influence of the wall boundary condition on a solution of the incompressible Navier–Stokes equations', *Technical Memorandum 42*, von Karman Institute, September 1986.
15. P. Gresho and L. Lee, 'Don't suppress the wiggles, they're telling you something', *Comput. Fluids*, **9**, 223–253 (1981).
16. K. Morgan, J. Periaux and F. Thomasset (eds), 'Analysis of laminar flow over a backward facing step, *Notes on Numerical Fluid Mechanics, Vol. 9*, Vieweg, 1984.
17. W. T. Thompkins and R. H. Bush, 'Boundary treatments for implicit solutions to Euler and Navier–Stokes equations', *J. Comput. Phys.*, **48**, 302–311 (1981).
18. R. W. MacCormack, 'Current status of numerical solutions of the Navier–Stokes equations', *AIAA Paper 85-0032. AIAA 23rd Aerospace Sciences Meeting*, Reno, Nevada, January 1985.
19. M. Napolitano and P. Orlandi, 'Laminar flow in a complex geometry: a comparison', *Int. j. numer. methods fluids*, **5**, 667–683 (1985).
20. U. Ghia, K. N. Ghia, S. G. Rubin and P. K. Khosla, 'Study of incompressible flow separation using primitive variables', *Comput. Fluids*, **9**, 123–142 (1981).
21. C. D. Tropea and R. Gackstatter, 'The flow over two dimensional surface-mounted obstacles at low Reynolds numbers', *ASME Trans., Series I: J. Fluids Eng.*, **107**, 489–494 (1985).
22. J. M. Leone and P. M. Gresho, 'Finite element simulations of steady, two dimensional viscous incompressible flow over a step', *J. Comput. Phys.*, **41**, 167–191 (1981).